Special Issue

3D Imaging of Retinal Pigment Epithelial Cells in the Living Human Retina

Zhuolin Liu, Omer P. Kocaoglu, and Donald T. Miller

School of Optometry, Indiana University, Bloomington, Indiana, United States

Correspondence: Zhuolin Liu, 800 E. Atwater Avenue, Bloomington, IN 47405, USA; liuzhuo@indiana.edu.

Submitted: January 9, 2016
Accepted: June 12, 2016

Citation: Liu Z, Kocaoglu OP, Miller DT. 3D imaging of retinal pigment epithelial cells in the living human retina. *Invest Ophthalmol Vis Sci*. 2016;57:OCT533–OCT543. DOI:10.1167/iovs.16-19106

Purpose. Dysfunction of the retinal pigment epithelium (RPE) underlies numerous retinal pathologies, but biomarkers sensitive to RPE change at the cellular level are limited. In this study, we used adaptive optics optical coherence tomography (AO-OCT) in conjunction with organelle motility as a novel contrast mechanism to visualize RPE cells and characterize their 3-dimensional (3D) reflectance profile.

Methods. Using the Indiana AO-OCT imaging system ($\lambda_c = 790$ nm), volumes were acquired in the macula of six normal subjects (25–61 years). Volumes were registered in 3D with subcellular accuracy, layers segmented, and RPE and photoreceptor en face images extracted and averaged. Voronoi and two-dimensional (2D) power spectra analyses were applied to the images to quantify RPE and cone packing and cone-to-RPE ratio.

Results. Adaptive optics OCT revealed two distinct reflectance patterns at the depth of the RPE. One is characterized by the RPE interface with rod photoreceptor tips, the second by the RPE cell nuclei and surrounding organelles, likely melanin. Increasing cell contrast by averaging proved critical for observing the RPE cell mosaic, successful in all subjects and retinal eccentricities imaged. Retinal pigment epithelium mosaic packing and cell thickness generally agreed with that of histology and in vivo studies using other imaging modalities.

Conclusions. We have presented, to our knowledge, the first detailed characterization of the 3D reflectance profile of individual RPE cells and their relation to cones and rods in the living human retina. Success in younger and older eyes establishes a path for testing aging effects in larger populations. Because the technology is based on OCT, our measurements will aid in interpreting clinical OCT images.

Keywords: retinal pigment epithelium, adaptive optics, optical coherence tomography, retinal imaging, photoreceptors

The retinal pigment epithelial (RPE) is a monolayer of cuboidal cells that lie immediately posterior to and in direct contact with photoreceptors. Retinal pigment epithelium has a fundamental role in the support and maintenance of photoreceptors and choriocapillaris. Its role is diverse, including nutrient and waste transport, reisomerization of all-trans-retinal, phagocytosis of shed photoreceptor outer segments, ion stabilization of the subretinal space, secretion of growth factors, and light absorption. It long has been recognized that dysfunction of any one of these can lead to photoreceptor degeneration and the progression of retinal disease, most notably age-related macular degeneration, but also Best's disease, Stargardt's disease, retinitis pigmentosa, and others.[1]

Much of what we know about the RPE and its interaction with photoreceptors comes either from in vitro studies using cultured RPE or animal models.[1–4] While these studies use powerful methods, they are invasive, ultimately destroying the tissue, and require extrapolation to not only the in vivo case, but to the human eye. Over the last three decades, noninvasive optical imaging methods have been established to probe properties of the RPE in the living human eye using autofluorescence,[5] multiply scattered light,[6–12] and thickness segmentation.[13,14]

In recent years, high-resolution adaptive optics (AO) imaging systems have advanced RPE imaging to the single cell level, providing first observations of individual RPE cells and cell distributions in the living human eye.[15] Such observations hold considerable promise to elucidating age-[2] and disease-related changes in RPE cell structure and density, both of which remain poorly understood. The ability to measure the same tissue repeatedly in longitudinal studies makes AO imaging systems attractive for assessing disease progression and treatment efficacy at the cellular level. Despite this potential and early success, however, RPE imaging remains challenging and has been largely confined to imaging select retinal locations of young, healthy subjects.

Regardless of AO imaging modality used, two fundamental properties of the retina inhibit RPE imaging: the waveguide nature of photoreceptors that obscure spatial details of the underlying RPE mosaic and the low intrinsic contrast of RPE cells. Direct imaging of RPE cells with AO scanning laser ophthalmoscopy (AO-SLO) has been demonstrated under restricted conditions where the photoreceptors are absent, as for example in localized regions of diseased retina,[16] and in the scleral crescent in the normal retina.[17] For the rest of the retina, other more advanced techniques are required. A dual-beam AO-SLO has been used with autofluorescence of lipofuscin[15,18] to enhance RPE cell contrast, providing the most detailed study to date of the RPE mosaic in the living primate eye. Extension of this method to more clinical studies, however, remains

Investigative Ophthalmology & Visual Science

challenged by the intrinsically weak autofluorescent signal and difficulty to image near the fovea owing to the strong excitation light that bleaches photopigment, causes subject discomfort, and is absorbed by the macular pigment. More recently, Scoles et al.[19] demonstrated direct resolution of the RPE mosaic using dark-field AO-SLO with near-infrared light, though leakage from adjacent choroid and photoreceptors reflections could not be eliminated.[19]

Adaptive optics optical coherence tomography (AO-OCT) also has been investigated[20,21] in large part because of its micrometer-level axial resolution that can section the narrow RPE band and avoid reflections from other retinal layers. However, speckle noise intrinsic to OCT masks retinal structures of low contrast, for example, RPE cells. Attempts to minimize this noise have included bandpass filters centered about the expected fundamental frequency of the RPE mosaic. These first AO-OCT approaches revealed the complexity of the problem and the need for improvements.

In this study, our solution was to combine AO-OCT with subcellular registration and segmentation. We found the combination of the two critical. First, this enabled us to segment contributions of RPE cells from rod outer segment tips (ROST), which for conventional OCT are unresolved and identified as a single band by the International Nomenclature for Optical Coherence Tomography Panel.[22] Second, it enabled us to average the registered RPE signal across time points sufficiently spaced that the natural motion of cell organelles enhanced cell contrast. With this method, we characterized the three-dimensional (3D) reflectance profile of individual RPE cells, including the contribution of ROST, as well as RPE cell packing geometry, and spatial relation to the overlying cone photoreceptors.

Methods

Description of AO-OCT Imaging System

The Indiana AO-OCT system used in this study has been described by Liu et al.[23] Relevant to this study, the AO-OCT system used a single light source, a superluminescent diode with central wavelength of 790 nm and bandwidth of 42 nm, for AO-OCT imaging and wavefront sensing. Nominal axial resolution of the system in retinal tissue ($n = 1.38$) was 4.7 μm with axial pixel sampling at 0.93 μm/px. The systems acquired A-scans at a rate of 250 KHz. The data stream from the system was processed and displayed using custom CUDA software developed for parallel processing by an NVIDIA Titan Z general purpose graphic processing unit.[24,25] Real-time visualization of A-scans, fast and slow B-scans, and C-scan (en face) projection views of the retinal layers of interest occurred at 20 frames per second.

Experimental Design and Subjects

Six subjects, ranging in age from 25 to 61 years (S1 = 25, S2 = 31, S3 = 35, S4 = 36, S5 = 48, and S6 = 61 years old) and free of ocular disease, were recruited for the study. All subjects had best corrected visual acuity of 20/20 or better. Eye lengths ranged from 23.56 to 26.07 mm (S1 = 24.04, S2 = 23.73, S3 = 24.96, S4 = 26.07, S5 = 25.4, and S6 = 23.56 mm) as measured with the IOLMaster (Zeiss, Oberkochen, Germany) and were used to correct for axial length differences in scaling of the retinal images following the method of Bennett et al.[26] All procedures on the subjects adhered to the tenets of the Declaration of Helsinki and were approved by the Institutional Review Board of Indiana University. Written informed consent was obtained after the nature and possible risks of the study were explained.

Intensity of the AO-OCT beam was measured at 400 μW at the cornea and below the safe limits established by the American National Standards Institute (ANSI)[27] for the retinal illumination pattern used and length of the experiment (details below). The right eye was cyclopleged and dilated with one drop of tropicamide 0.5% for imaging and maintained with an additional drop every hour thereafter. The eye and head were aligned and stabilized using a bite bar mounted to a motorized XYZ translation stage.

Adaptive optics OCT volumes were acquired at two retinal locations, 3° and 7° temporal to the fovea, on all subjects. These locations were selected as the RPE is known to have different concentrations of melanin and lipofuscin, and, thus, may provide a means to differentiate light scatter contributions from the two organelles. Concentrations follow an inverse relation with melanin peaking in the fovea and lipofuscin in the periphery, generally at 7° or beyond.[3,28,29] This inverse relation is largely age-independent albeit the overall concentrations of melanin and lipofuscin are age-sensitive with melanin decreasing and lipofuscin increasing. While imaging the foveal center would have maximized the difference in melanin concentration with that at 7°, AO-OCT images at 3° are easier to process because the AO-OCT scan pattern is less distracting to the subject and results in less eye motion artifacts. For each retinal location, 30 to 35 AO-OCT videos (each ~4 seconds in duration) were acquired at 3-minute intervals over approximately 90 minutes. For one subject (S5), the 90-minute experiment was repeated 2 days later resulting in a total of 64 AO-OCT videos for that subject's 3° location. Each video consisted of 10 volumes acquired at a rate of 2.8 Hz. Volumes were 1° × 1° at the retina and A-scans sampled at 1 μm/px in both lateral dimensions. A fast B-scan rate of 833 Hz reduced, but did not eliminate, eye motion artifacts.

Before collection of the AO-OCT volumes, system focus was adjusted to optimize cone image quality, determined by visual inspection of cones in en face images that were projected axially through the portion of the AO-OCT volume that contained the cone inner/outer segment junction (IS/OS; also called the ellipsoid zone[22,30]) and cone outer segment tip (COST) reflectance bands.[31]

3D Image Registration and Data Analysis

Three-dimensional registration was applied to the entire AO-OCT volume, followed by layer segmentation and data analysis to the following four principle reflections: IS/OS, COST, ROST, and RPE. These three processing steps were realized with custom algorithms developed in MATLAB (Mathworks, Natick, MA, USA). Registration and segmentation were based upon our previously published registration algorithms,[32,33] and data analysis algorithms were new for this study.

The best AO-OCT volume of each 10-volume video was selected based on the criteria of cone visibility in the en face projection, minimal eye motion artifacts, and common overlap with the other volumes selected for the same retinal location. For some time points that we imaged, we could not meet this selection criteria and therefore, volumes were not selected for these points. This selection resulted in 24 to 35 volumes for each retinal location with subject S5 having 64 volumes for 3° because of the additional imaging session. All further processing was applied to these selected volumes.

Critical in our method to individuate RPE cells was correction of eye motion artifacts in all three dimensions as these can be many times larger than the cellular features we wanted to extract from the volumes. For axial segmentation, we first registered each A-scan in the AO-OCT volume using a

Investigative Ophthalmology & Visual Science

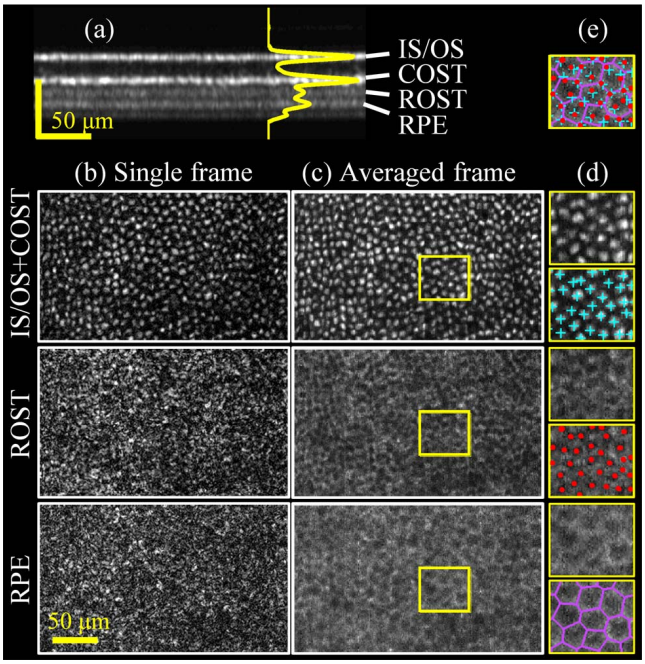

Figure 1. Adaptive optics OCT cross-sectional and en face images extracted from the photoreceptor-RPE complex in a 25-year-old subject (S1) at 7° temporal retina. (**a**) Averaged B-scan and corresponding A-scan profile of a registered AO-OCT volume reveal distinct reflectance bands within the complex labeled IS/OS, COST, ROST, and RPE. En face projection views of (**b**) single and (**c**) averaged registered frames are shown for IS/OS + COST, ROST, and RPE layers. For brevity, IS/OS and COST are shown combined due to their similar appearance.[34,38] Averaged, registered frames reveal darkened cone projections that are surrounded by a halo of elevated reflectance at ROST. A similar pattern occurs at RPE, but of coarser grain and no apparent relation to the cone mosaic. (**d**) Magnified views of the *yellow* highlighted subregion in (**c**) provide better visualization of cellular detail. For comparison, copies of the magnified images also are shown with cell locations marked. (**e**) The same magnified cone view is shown with all three marks superimposed. In the Supplementary Video S1, frames #14, #24, #30, and #35 pertain to IS/OS, COST, ROST, and RPE, respectively. As expected at 7° retinal eccentricity, the cone reflection at IS/OS (#14) appears multimodal and at COST (#24) single mode.[34] *Scale bar*: 50 μm.

two-step iterative cross-correlation method. Next, the IS/OS, COST, ROST, and RPE layers were identified in each A-scan using an automated algorithm based on multiple one-dimensional cross-correlations.[32]

Next, lateral eye motion was corrected using our stripe-wise registration algorithm that we had validated previously for investigations into cone photoreceptor temporal properties.[32,33] Because all pixels along an A-scan are acquired simultaneously, eye motion is the same along the entire A-scan. Thus, registration of the ROST and RPE images entailed stripe-wise registration of the projected cone layers (IS/OS + COST) from which registration coordinates then were applied directly to the underlying ROST and RPE layers. In principle we could have applied the stripe-wise registration directly to ROST and RPE, but lack of robust image features in either case made this difficult and there was little benefit to do so.

Finally, the motion-corrected cone (IS/OS + COST), ROST, and RPE images were averaged across the selected volumes to generate averaged, registered en face images for cone, ROST, and RPE, an example of which is given in Figure 1. For reference purposes, the depth at which the en face images were extracted was measured relative to the IS/OS layer (zero location). The IS/OS was selected as the reference depth owing to its strong reflectance and narrow axial extent.

The geometric arrangement of cone and RPE cells was analyzed using Voronoi maps, a mathematical construct frequently used for quantifying cell association in retina tissue.[3,15,16,19] Voronoi maps were generated using cone cell centers that were identified automatically in the AO-OCT images using previously described MATLAB code.[32] Retinal pigment epithelial cell centers were selected manually. From these maps the following metrics were computed: Nearest neighbor distance (NND), number of nearest neighbors, mean of Voronoi side lengths, mean standard deviation of Voronoi side lengths, Voronoi cell area, cell density, and cone-to-RPE ratio. Cell density was defined as the ratio of total number of RPE cells (selected cells in the Voronoi maps) to total area of RPE cells (summation of the selected cell areas). Cone-to-RPE ratio was defined as the ratio of cone to RPE cell densities.

Two-dimensional (2D) power spectra were computed of the cone, ROST, and RPE en face images and served three purposes: to compare frequency content of the three layers, quantify average RPE cell spacing and density, and determine signal-to-noise ratio (SNR) of the RPE signal in the images. Cell spacing was determined from the radius of the ring of concentrated energy in the power spectra corresponding to the cone and RPE mosaic fundamental frequencies. All conversions to row-to-row spacing assumed triangular packing. The SNR was defined as the RPE peak signal (cusp of concentrated energy) divided by the average noise floor in the power spectrum, and was calculated for different numbers of images averaged (1, 10, 24, and maximum images registered).

Additional 3D Data Analysis

To further characterize the ROST reflectance and axial separation of IS/OS, COST, ROST, and RPE with retinal eccentricity, AO-OCT data from a previously reported experiment[34] were reanalyzed for subject S5. In that study, AO-OCT volumes were acquired at eight retinal eccentricities along the temporal horizontal meridian (0.6°, 2°, 3°, 4°, 5.5°, 7°, 8.5°, and 10°). The additional retinal eccentricities (eight instead of two) and finer A-scan sampling (0.6 instead of 1.0 μm/px) provided better assessment of rod presence with eccentricity (including the rod-free zone[35]) and individuation of rods. Best focus was placed at the photoreceptor layer. Note that because volume videos were acquired at effectively only one time point for each retinal location, the RPE cell mosaic could not be assessed.

At each retinal location, 10 AO-OCT volumes of the same video were axially registered and then from each an averaged A-scan and projected fast B-scan computed. For each A-scan, the IS/OS, COST, ROST, and RPE peak locations were identified manually and their depth location determined relative to IS/OS. Depth location was averaged over the 10 volumes. From the best volume (least apparent motion artifacts), en face images were extracted of cone and ROST layers, and then superimposed as a false-color image denoting depth.

Results

3D Imaging of Photoreceptor-RPE Complex

Volumetric patches of retina were successfully imaged and registered in all six subjects and two retinal eccentricities. Representative single and averaged, registered images acquired at 7° retinal eccentricity in one subject are shown in Figure 1 (Supplementary Video S1 shows en face flythrough of the averaged, registered volume). The averaged B-scan and averaged

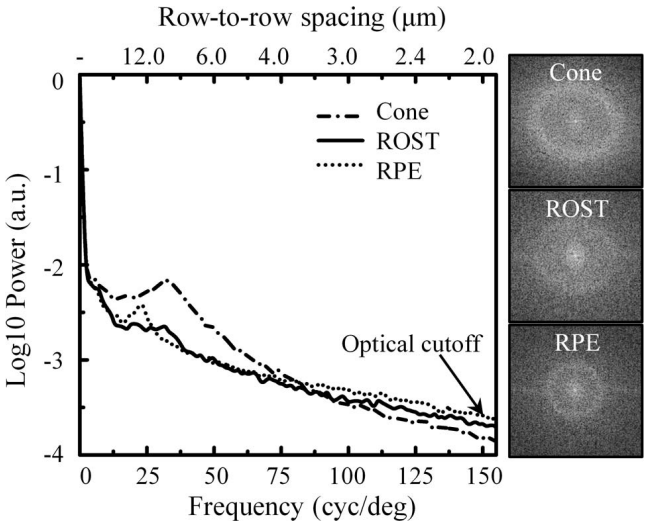

Figure 2. Power spectra of en face images of Subject 1 at 7° temporal retina. *Left*: Circumferential-averaged power is shown for cone (*dash dot*), ROST (*solid*), and RPE (*dot*) layers. *Right*: Two-dimensional power spectra displayed as grayscale image. To better visualize the ring of concentrated energy, the 2D power spectra are cropped at 56 cyc/deg (5.3 μm spacing).

A-scan profile in Figure 1a reveal distinct reflectance bands within the photoreceptor-RPE complex. These are labeled IS/OS, COST, ROST, and RPE with their corresponding single-frame en face projections shown in Figure 1b. As expected, the single en face frame (Fig. 1b, top) reveals a regular pattern of bright punctate reflections, each originating from an individual cone cell and consistent with that reported previously with AO-OCT.[21,31,32,34,36–38] Unlike the cone reflection, a regular pattern is not evident in single-frame images of the ROST (Fig. 1b, middle) and RPE layers (Fig. 1b, bottom). However, a pattern emerges when registered images of the same patch are averaged. This is illustrated in Figure 1c (middle and bottom) for the averaging of 26 frames. Rod outer segment tips and RPE layers reveal a regular pattern, but with reflectance inverted from that of cones, that is, darkened punctate reflections in a bright surround. The ROST and RPE appear similar, not unexpected given they originate within the conventional RPE reflectance band[22,30] and are separated in depth by just 10 μm.

Table. Measured Row-To-Row Spacing Based on Analysis of Power Spectra in Figure 4

	S1	S2	S3	S4	S5	S6	Mean ± SD
3°, μm	13.4	12.2	13.3	15.5	14.4	14.0	13.8 ± 1.1
7°, μm	12.8	13.0	13.4	14.6	14.0	14.3	13.7 ± 0.7

However, on closer inspection, the two mosaic patterns are spatially distinct, in terms of the location and spacing of the darkened punctate reflections. These differences, as well as those with the overlying cone mosaic pattern, are evident in Figures 1d and 1e. To aid the comparison, the bright spots in the cone projection and dark spots in the ROST and RPE layers (see Fig. 1d) are manually marked. Figure 1e demonstrates the one-to-one correspondence between cone (cyan cross) and darkened spot (red dot) in the ROST, with a psuedo-shadow typically forming underneath each cone. In contrast no correspondence is apparent between cones (or equivalently their psuedo-shadow locations in ROST) and RPE (purple Voronoi map). In fact, for the magnified view shown, there are approximately two times more cones (bright spots) than dark spots in RPE.

Figure 2 shows power spectra of the en face images in Figure 1 (cone projection, ROST, and RPE layers). Rings of concentrated energy are evident in the three power spectra, substantiating the observation of regular mosaics in the en face images of Figure 1c. However the rings of ROST and RPE locate at different frequencies in the power spectra, supporting the observation of different spatial cell arrangements in the two layers. The circumferential-averaged power spectra of cone and ROST (which has a less distinct cusp of energy) have local maxima at 31.8 cyc/deg (row-to-row spacing of 9.4 μm assuming triangular packing), while that of RPE has a local maxima at 23.4 cyc/deg (row-to-row spacing of 12.8 μm).

Averaged, registered RPE images from all six subjects and at both retinal eccentricities are displayed in Figure 3. While faint, a regular pattern of darkened spots is present in the 12 RPE images along with a concentrated ring of energy in the corresponding 2D power spectra. A more quantitative view of the power spectra is shown in Figure 4, plotted as circumferential-averaged power with intersection of the ring evident as a

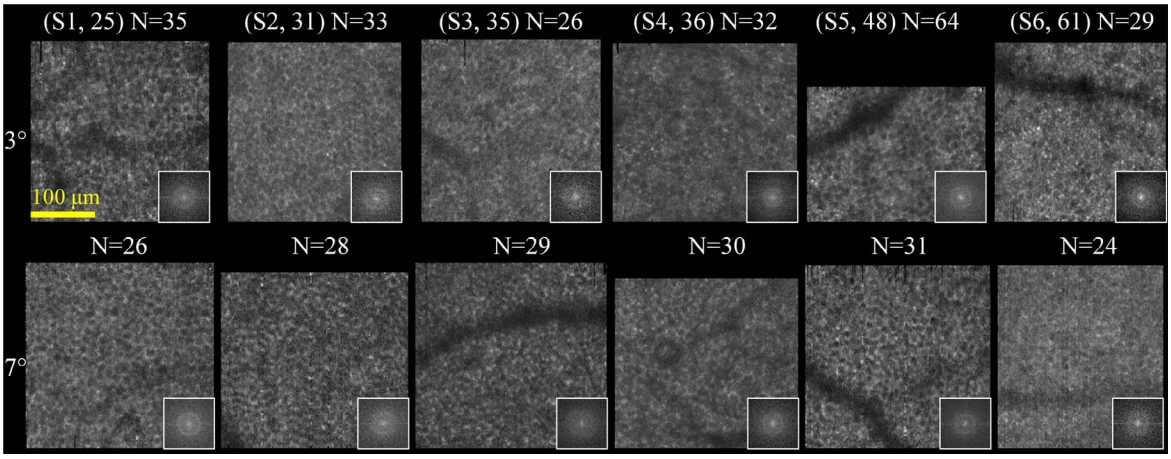

Figure 3. Averaged, registered RPE images for all six subjects imaged at 3° (*top*) and 7° (*bottom*) temporal to fovea. Corresponding 2D power spectra reveal rings of concentrated energy whose radii are consistent with RPE cell spacing. Subjects are ordered by increasing age. *N* is the total number of images averaged. Image size varies with overlap of the images. Note that some power spectra contain a line of elevated power along the horizontal meridian, an artifact due to the stripe-wise registration method used.

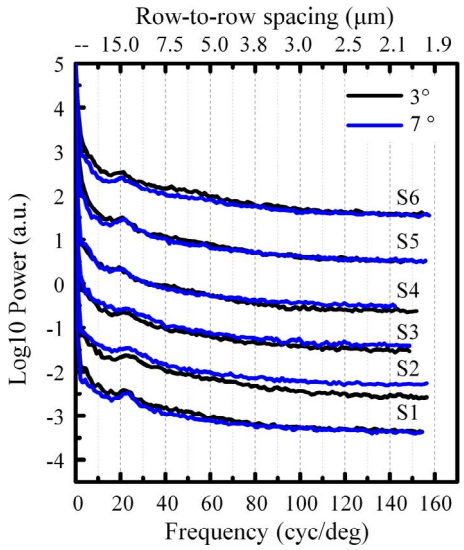

Figure 4. Circumferential averages of the twelve 2D power spectra displayed in Figure 3. Cusps in the traces denote the fundamental frequencies of the darkened spot arrays in RPE images, which were interpreted as the RPE cell mosaic. For visualization purposes, spectra are normalized to the same DC level and displaced vertically in groups by subject.

cusp in the trace. Assuming triangular spacing, the Table converts these peak (fundamental) frequencies to row-to-row spacings resulting in 13.8 ± 1.1 (3°) and 13.7 ± 0.7 (7°) μm for the six subjects. These spacings are consistent with that expected of the RPE cell mosaic. Given that we know of no other cellular structure at this depth in the retina with this regularity, we interpret the mosaic to be the RPE cell mosaic and each darkened spot in the mosaic to be an individual RPE cell.

To better characterize the retinal eccentricity dependence of ROST and RPE, Figure 5 presents our reanalysis of previously reported AO-OCT data on subject S5. Across the eight retinal eccentricities imaged, clear and systematic differences in ROST reflectance and axial separation of the layers are evident in cross-section (averaged A-scan and B-scan) and en face views.

Voronoi Analysis of RPE Layer

Voronoi analysis was applied to the RPE images to determine packing properties of the RPE cell mosaic. To illustrate, Figure 6 shows the cone and RPE cell mosaics from the same averaged, registered AO-OCT volume acquired 3° temporal to fovea of Subject 5. The photoreceptor and RPE cell mosaics are shown in Figures 6a and 6b, respectively. As evident in the Figure, the RPE cell mosaic is more coarsely tiled than the cone mosaic of the same retinal patch. For analysis, cell locations of each cell type were identified as depicted in Figures 6c and 6d. Difference in density and area of the two cell types are evident when cell centers of the two are superimposed (Fig. 6e). Using cone centers and Voronoi mapping of the RPE mosaic, the average number of cones per RPE cell for this retinal patch is 4.0:1. Superposition of the 2D power spectra of the two layers demonstrates a clear difference in fundamental frequency denoted by the two rings of concentrated power (Fig. 6f). Corresponding row-to-row spacing is 7.2 and 14.4 μm for cones and RPE cells, respectively, confirming the spatially coarser tiling of the RPE cells.

As illustrated by the constructed 3D view in Figure 7 (Supplementary Video S2 shows 360° rotational view of the same volume), simultaneous imaging of the RPE and cone layers by AO-OCT enables volume rending with true one-to-one mapping of cellular structures at different depths. In this case the Voronoi map is superimposed at the depth of RPE and enables the number of cones per RPE cell to be computed.

Because of potential subjectivity in our Voronoi analysis due to the manual selection of RPE cell centers, we tested for agreement between two trained technicians who independently mapped

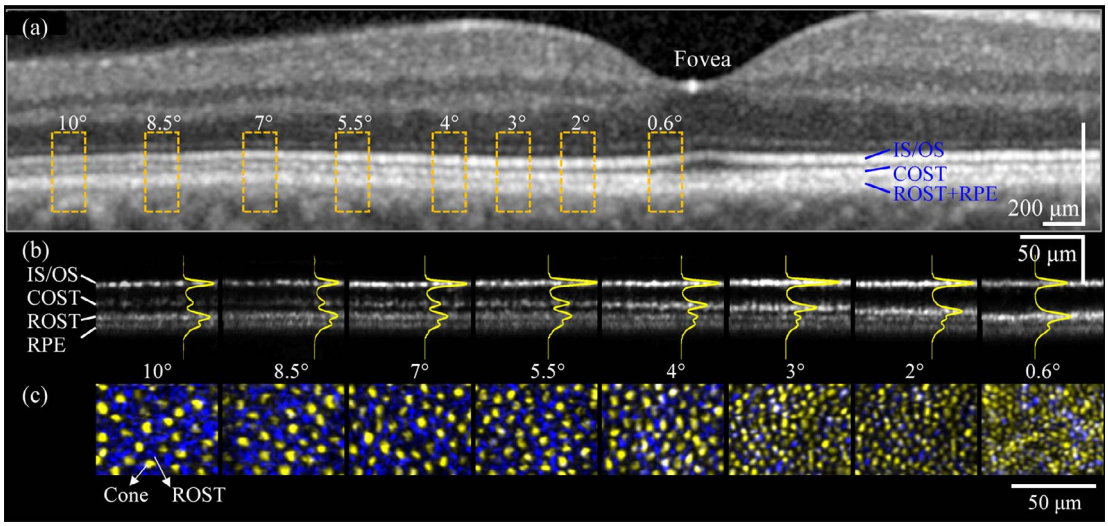

Figure 5. Adaptive optics OCT cross-sectional and en face images extracted from the photoreceptor-RPE complex of a 48–year-old subject (S5) at eight retinal eccentricities. (**a**) Clinical OCT is shown for comparison, a Spectralis OCT B-scan that bisects the fovea along horizontal meridian of the same subject. IS/OS and COST bands are distinct, but RPE and ROST bands are undifferentiated. (**b**) Adaptive optics OCT averaged B-scans and corresponding A-scan profiles (*yellow trace*) of volumes reveal distinct reflectance bands within the complex labeled IS/OS, COST, ROST, and RPE. Note the increase in ROST peak with retinal eccentricity. (**c**) En face projection views of single frames are shown with depth color coded; that is, IS/OS + COST (*yellow*) and ROST (*blue*) layers. The *blue* punctate reflections are consistent with individual rods that surround cones (*yellow*), which themselves become increasingly larger outside the fovea and displace adjacent rods. *White* denotes overlap of cone and rod reflections, which, while infrequent, occurs at retinal locations closer to fovea. This apparent overlap is likely attributable to limitations in the AO-OCT resolution and segmentation of COST and ROST, cell end tips that get increasingly narrow and close together in the fovea.

Investigative Ophthalmology & Visual Science

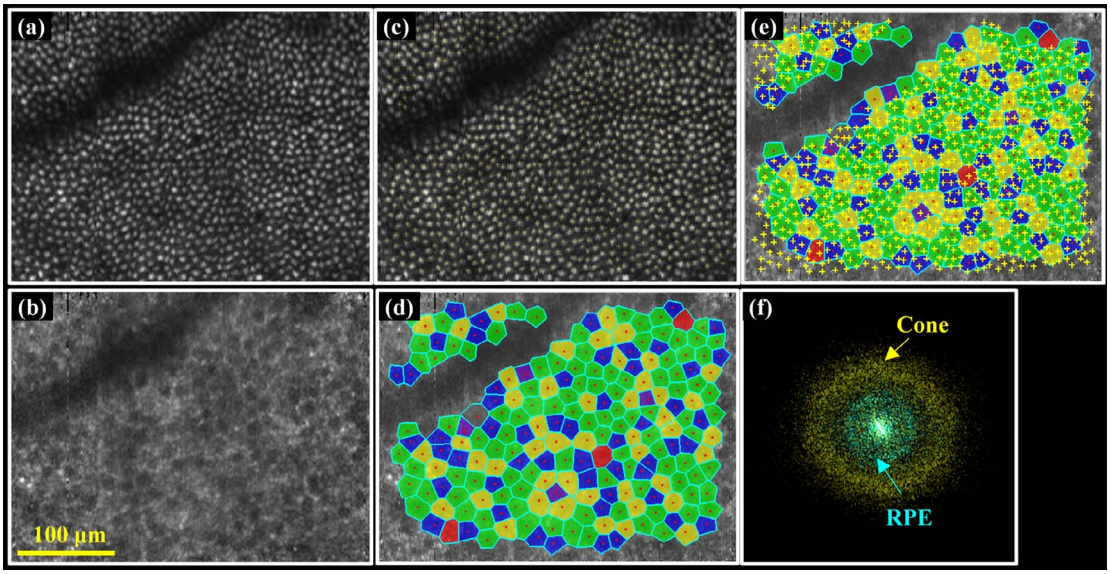

Figure 6. Voronoi and power spectral analysis applied to averaged, registered (**a**) cone and (**b**) retinal pigment epithelium images of Subject 5 at 3° temporal retina. Averaging contained 64 frames. (**c**) Identified cone centers are superimposed on cone image in (**a**) and marked with *yellow crosses*. (**d**) Retinal pigment epithelium Voronoi map is superimposed on RPE image in (**b**), and RPE cell centers are marked with *red dots*. Color key for number of nearest neighbors is: *purple*: 4, *blue*: 5, *green*: 6, *yellow*: 7, and *red*: 8. (**e**) To compare difference in cell distribution, cone and RPE cell centers in (**c**) and (**d**) are superimposed on RPE image in (**b**). (**f**) Two-dimensional power spectra of (**a**) and (**b**) are superimposed and color coded (RPE cells, *cyan;* cones, *yellow*).

RPE centers in all six subjects and two retinal locations. Of these 12 datasets, we found one (S3, 7°) outlier that yielded a difference in measured density of 29% between technicians and fell outside the 95% confidence range of a Bland-Altman test. Average absolute difference between the other 11 was 3.4% in terms of cell density and 1.8% when converted to cell spacing assuming triangular packing. Based on this test and the observation that RPE cells in the (S3, 7°) image were notably less clear than in the others, we excluded this image from the Voronoi analysis. Note that while manual cell identification was determined unreliable for this image, its power spectrum still yielded a ring of energy at the expected RPE frequency (see Figs. 3, 4).

Results of our Voronoi analysis are summarized in Figures 8 to 10, which show RPE number of nearest neighbors, Voronoi side length, cell area, cell density, and cone-to-RPE ratio for the six subjects and two retinal eccentricities imaged. Analysis is based on a total of 2997 RPE cells.

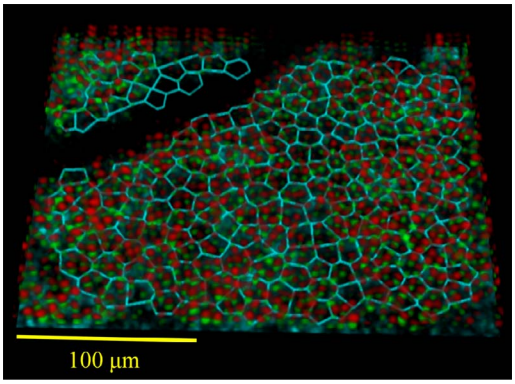

Figure 7. Adaptive optics OCT volumetric reconstruction of the photoreceptor-RPE complex on Subject 5 at 3° temporal to fovea. *Red* and *green spots* denote reflections from opposing ends of individual cone photoreceptor outer segments (IS/OS in *red* and COST in *green*). A Voronoi map of the underlying RPE cells (*cyan*) is superimposed at the depth of RPE (see Supplementary Video S2).

Discussion

3D Reflectance Profile of Photoreceptor-RPE Complex

Our AO-OCT study revealed that the RPE band observed in conventional OCT is actually composed of two distinct, but

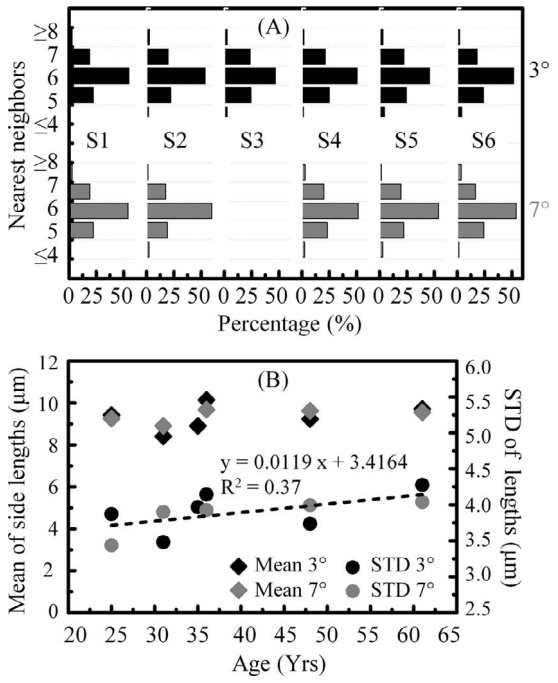

Figure 8. (**A**) Prevalence of nearest neighbors of RPE cells across subjects and retinal eccentricities examined. (**B**) Mean and mean standard deviation of the Voronoi side lengths are plotted as function of subject age.

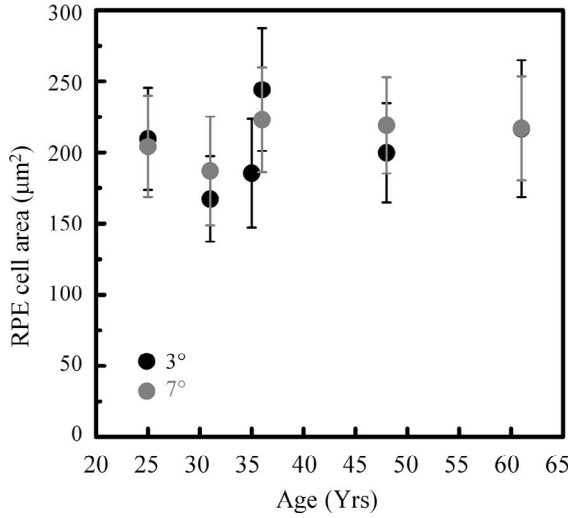

Figure 9. Average RPE cell area at 3° (*black*) and 7° (*gray*) temporal to the fovea in the six subjects. *Markers* and *error bars* are the average and standard deviation of the measured Voronoi areas, respectively.

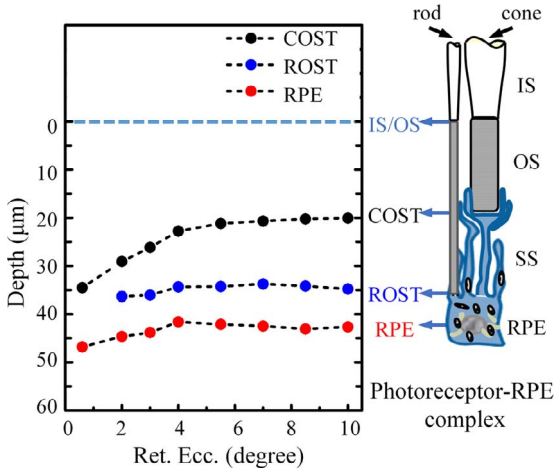

Figure 11. Axial displacement of COST, ROST, and RPE from IS/OS as a function of retinal eccentricity. Displacements were measured on a 10-volume average at each of the eight retinal eccentricities of S5. Schematic on *right* depicts depth location of the four main reflections in the Photoreceptor-RPE complex used in this study.

faint bands. Both bands were visible regardless of age and separated in depth by approximately 10 μm (see Fig. 1a). We labelled these as ROST and RPE. Other AO-OCT and OCT studies also have reported two subbands in the RPE layer[21,37,39] and appear to correspond to ROST and RPE in this study. However, unlike these other studies, we observed the double band in every subject (6 subjects) and retinal location (3° and 7° in the six subjects and 2° to 10° in one subject) imaged, except near the foveal center, that is, 0.6°. This suggested that the double band is likely present across much of the retina, further supported by the fact that the band appears to depend on fundamental properties of rods and RPE cells (discussed below).

It should be noted that in the younger eyes an additional more posterior band also is apparent, thus, making the double band actually a triple band, as for example Figure 1a, which shows a faint band immediately below that labeled RPE. In older subjects, this additional band is not evident, for example in Figure 5. The additional band is likely attributable to Bruch's membrane, but further analysis is required and beyond the scope of this study. Here, we limited our analysis to the dual band.

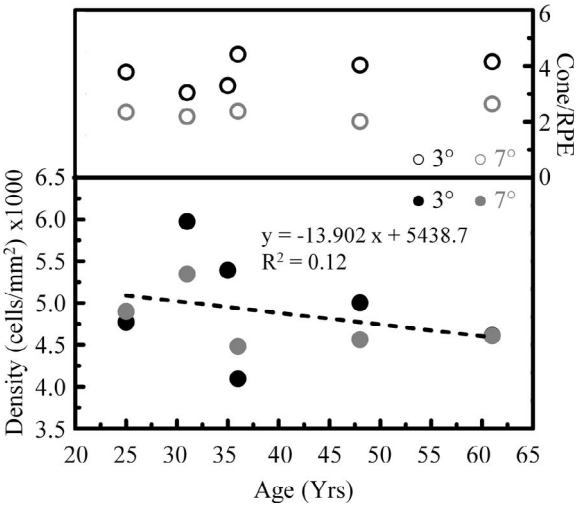

Figure 10. Retinal pigment epithelial cell density and cone-to-RPE ratio are shown as a function of subject and retinal eccentricity.

Our best characterization of the depth profile of the dual band is with the AO-OCT measurements in Figures 5 and 11, obtained on Subject S5 from 0.6° to 10° retinal eccentricity. These measurements reveal not only the variation in the ROST peak with retinal eccentricity, but also the peak's axial separation from other prominent reflections in the photoreceptor-RPE complex, namely IS/OS, COST, and RPE. As shown in Figure 11, the ROST-to-IS/OS separation (defined as the rod OS length) is relatively constant across retinal eccentricities, on average 34.81 ± 0.99 μm, which is consistent with the histologic value of 32 μm summarized by Spaide and Curcio,[30] but shorter than the 40 to 45 μm reported near the optic disc using ultrahigh-resolution OCT.[39] In contrast the COST-to-IS/OS separation decreases from 29.07 to 20.07 μm over the same retinal eccentricity range, a 31% reduction and consistent with histology.[40] The subcellular space (SS) between ROST and COST increases from 7.27 μm at 2° to 14.71 μm at 10°, while the separation between ROST and RPE remains relatively constant at 8.11 ± 0.58 μm regardless of retinal location. Across all six subjects in our study, the separation between ROST and RPE was 8.93 ± 1.00 μm. This separation does not necessarily correspond to actual RPE thickness, but is consistent with histologic values of thickness reported in the macula (10.3 ± 2.8 μm).[28]

Closer examination of the double band (ROST and RPE) reveals that neither is a true band, that is, exhibiting uniform reflectance, but instead consists of spatially distinct mosaics of different grain. The ROST mosaic is characterized by darkened punctate reflections in a bright surround, with the darkened spots lying under cones, thus, appearing as cone (pseudo-) shadows. This arrangement was observed in all subjects examined though varied with retinal eccentricity. While not apparent in the averaged images, numerous single images and, in particular, those acquired in S5 using finer A-scan sampling of 0.6 μm/px (see Fig. 5c), revealed the bright surround was pixeled with many punctate reflections (blue) that our system could only partially individuate, a size suggestive of rod photoreceptors. This observation of rod structure is consistent with earlier AO-OCT reports of rod-like reflections at this retinal depth.[21,23,37] A reflection at this depth also is consistent

Investigative Ophthalmology & Visual Science

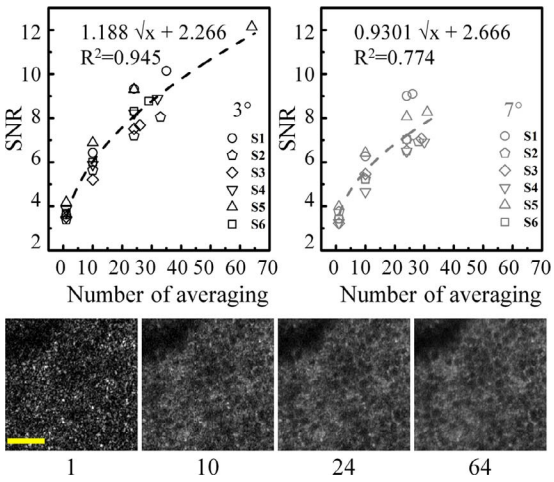

Figure 12. Signal-to-noise ratio of RPE fundamental frequency at (*top left*) 3° and (*top right*) 7° retinal eccentricity as a function of AO-OCT images averaged. Retinal pigment epithelium fundamental frequency and noise were determined from the power spectrum of the registered, averaged image. Images were acquired at 3-minute intervals. Signal-to-noise ratio increase follows the square root of the number of images (*dashed curves*). *Bottom*: Representative RPE images of the same retinal patch for one subject (S5) are shown with different levels of averaging (1, 10, 24, and 64 of images). *Scale bar*: 50 μm.

with where rod outer segments abut the RPE cell bodies based on histology.[30]

As further evidence of a ROST attribution, the punctate reflections become increasingly more prevalent with increased retinal eccentricity as shown by the increase blue regions in Figure 5c. Note that traces of blue – albeit small – appear at 0.6°, which lies within the rod-free zone.[35] This is likely not attributable to rods, but rather the inability of our method to separate COST from the apical portion of the RPE due to their increasingly close proximity in the foveal region. Prevalence of ROST also can be assessed by its reflectance in cross-section, as for example in the averaged B-scan and A-scan profiles of Figure 5b. As evident in the yellow A-scan traces, the ROST reflectance peak increases monotonically with retinal eccentricity starting with no evidence of a ROST peak at 0.6° and a substantive one at 10°, resulting in the second strongest peak in the entire A-scan profile. This trend is consistent with what we know of rod density, absent near the fovea and increasing outward with a maximum density at 15° to 20° retinal eccentricity.

In general our findings suggested that ROST is a superposition of two mosaics, a coarse one created by cone (pseudo-) shadows and a much finer one created by rod OS tip reflections.

The RPE mosaic also consisted of darkened spots in an elevated surround, but of coarser grain and no apparent relation to the cone mosaic. This finding should not be unexpected given the basal location of the RPE cell nuclei and match of the darkened spot spacing to that of RPE cells (see cell density comparison below). The darkened spots likely correspond to the cell nuclei since their low refractive index ($n \sim 1.4$; Ref. 41) relative to surrounding organelles (e.g., melanin at $n \sim 1.7$) and their large size ($\gg\lambda$) results in highly anisotropic scatter (strong forward scatter and weak back scatter). In addition, size of the darkened spots compared favorably to that reported with other in vivo imaging modalities[15,19] and with histology.[3,42] It should be noted that an alternative explanation is that the darkened spots are generated by clusters of melanin granules – rather than RPE nuclei – which apically shield the nuclei from light exposure.[4,43] This explanation seems plausible at visible wavelengths where melanin absorbs strongly, but at the near infrared wavelengths of our AO-OCT, melanin absorption is at least 7 times less.[44]

The elevated reflection that surrounds the darkened spots most likely originates from scatter of organelles in the cytoplasm, the predominate ones being melanin and lipofuscin granules. Of these, melanin is known to be a strong scatterer owing in part to its high refractive index ($n \sim 1.7$). In addition, growing evidence points to melanin as the source of the strong OCT signal in the RPE layer.[13,45] This makes melanin the likely source of the elevated surround in our images. Consistent with this expectation is the higher SNR we measured for RPE cells at 3° compared to at 7° (see Fig. 12 and discussion in next section). Because of the inverse concentration of melanin and lipofuscin with retinal eccentricity,[28] we would expect the opposite, that is, higher contrast at 7°, had lipofuscin been the key scatterer. A further test would have been to analyze reflectance of the cytoplasm as a function of depth in the RPE cell as melanin and lipofuscin also are nonuniformly distributed in this dimension.[28,29] However, the ROST reflection in the apical half was too strong and masked contributions of organelles there.

Based on this collection of evidence, we interpreted the mosaic observed in the RPE band to be the RPE cell mosaic.

Organelle Motility and Volume Averaging

We found volumes acquired over 90 minutes at 3-minute intervals generated different noise patterns across the RPE image, suggesting this time interval was long enough for sufficient organelle (e.g., melanin) motility to occur. Averaging these volumes reduced the prevalence of noise and increased the RPE cell signal, which increased clarity of the RPE mosaic. In contrast, we observed little improvement in RPE cell clarity when volumes acquired over seconds (<6 seconds) were averaged, as opposed to minutes. While it remains to be determined what the optimal timing acquisition parameters should be, we can gain insight into the benefit that accrues from averaging. To do this, we systematically computed SNR for the RPE mosaic as a function of number of images averaged across subjects and retinal eccentricities.

Figure 12 plots the results of the SNR analysis along with representative RPE images of different averaging. As evident in the plot, SNR improves proportional to the square root of images averaged, expected if the noise patterns are independent. More images always resulted in higher SNR, indicating that images were registered with an accuracy better than the size of RPE cells. In fact, averaging over two 90-minute sessions (S5, 3°) provided the highest SNR. Visual inspection of the averaged images found those with the best RPE mosaic clarity had the highest SNR. Our results indicate that even more averaging than we had done will benefit RPE cell clarity, but this comes at the expense of longer image acquisition, which imposes a practical limit.

In this study, we did not optimize the time required to perform the experiment and process the images, an important consideration for assessing clinical utility. Data collection was over 90 minutes followed by several hours of postprocessing and data mining of the images. While obviously too long to be of clinical benefit in the current form, we anticipate the total time can be decreased substantially. In fact, we have recently demonstrated the same number of images can be captured in one-third the time, that is, 30 instead of 90 minutes, without loss in RPE cell clarity, and even shorter times appear possible (Liu Z, et al. *IOVS* 2016;57:ARVO E-Abstract 2807). As for postprocess-

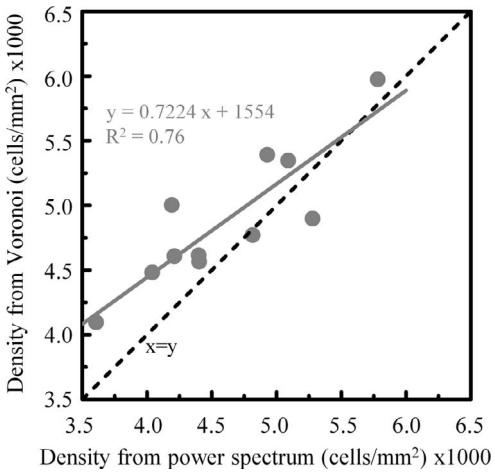

Figure 13. Correlation of RPE cell density determined from Voronoi and power spectrum analyses. Included are measurements on all six subjects and two retinal eccentricities except (S3, 7°). For reference, the *black dashed line* denotes a slope of one, and the *gray solid line* is the linear regression fit.

ing, we see no fundamental limit that prevents reducing the principle steps of image registration, RPE cell identification, and Voronoi and spectral analysis using more powerful data processing tools, such as parallel computing. Also, while some of the steps already are automated (e.g., Voronoi and spectral analyses), others are not, in particular RPE cell identification, which was done manually. Automating identification would lead to further reductions.

RPE Mosaic Characterization Using Voronoi and Power Spectra Analyses

Cell density measurements from power spectra and Voronoi are sensitive to different properties of the mosaic regularity. The former is sensitive to the dominant cell packing frequency and the latter to local variations in the frequency and irregularities at the cell level. To determine the extent to which these differences manifest themselves for density measurements of the RPE mosaic, we tested their correlation on the same images. Results are shown in Figure 13 and reveal an R^2 of 0.76. Average absolute difference between measurement points in the Figure is 9.4% of the average cell density, corresponding to a difference in row-to-row cell spacing of 0.64 μm assuming triangular packing. While this average difference is relatively small, individual differences from the same RPE image are notable in the plot and do not appear systematic. In general Voronoi estimates a higher density than power spectra, perhaps because local irregularities in the mosaic are of generally finer fidelity. Interestingly, we processed RPE images from the study of Morgan et al.[15] using power spectra and when compared to their reported Voronoi density measurements found a similar trend.

Comparison to Other RPE Studies

It is difficult to compare our RPE density measurements to other studies owing to differences between subjects, retinal locations, and age, but a few notable comparisons are made here. To facilitate, we chose to use density measurements from the Voronoi analysis instead of power spectra as the former better aligns to the methods used in the literature, some of which were based on Voronoi. From our Voronoi analysis, average RPE cell density for the six subjects at 3° and 7° temporal retinal eccentricity (Fig. 10) were 4975 ± 651 cells/mm² and 4780 ± 354 cells/mm², respectively. Two in vivo imaging studies used autofluorescence AO-SLO[15] and dark-field AO-SLO[19] to image RPE cells in normal, relatively young subjects. For autofluorescence AO-SLO, three subjects (25–30 years) were imaged along the superior vertical meridian starting at 5°, 6.25°, and 15° from fixation. Retinal pigment epithelium density at the most relevant locations of 5°, 6.25°, and 7.5° in two subjects ranged from 5090 to 5970 cells/mm² with an average of 5645 cells/mm², which is elevated compared to the 4780 ± 354 cells/mm² measured at 7° in the present study. Analysis of the same AO-OCT volumes, but at the photoreceptor layer yielded cone density measurements of 11,032 ± 1174 cells/mm² that is consistent with histology[35] and in vivo[46] cone packing studies. This suggests the source of the RPE difference is unlikely to be caused by an error in our AO-OCT system, image acquisition, or common data processing steps for RPE and cone cells. For dark-field AO-SLO, seven subjects (19–40 years) were imaged at the foveal center and 10° temporal to fixation with measurements limited to NND. While our 3° measurements were too distant to compare to foveal densities, our average NND at 7° was 12.2 ± 1.6 μm compared to 13.4 ± 0.6 μm at 10° by Scoles et al.[19] The difference between these two is not statistically significant ($P > 0.05$).

From histology considerable variation has been reported. Panda-Jonas et al.[47] measured RPE density in 53 eyes confined to annuli concentric to the fovea. In the first annulus (2–5 mm, or approximately 6.7°–16.7°) density along the temporal meridian was 3392 ± 528 cells/mm². While average age (58.6 years) was higher than in the present study (39.3 years), accounting for the 0.3% decrease per year as observed by Panda-Jona et al.[47] decreases our 7° measurements to 4503 cells/mm², which is still 33% higher. However, Watzke et al.[48] reported RPE density in 20 normal eyes, 10 below the age of 50 years for two retinal locations that straddle our 3° and 7° measurements. They report 5893 ± 809 cells/mm² within 250 μm of fovea (<1°) and 4834 ± 764 cells/mm² at 4 mm (∼13.3°) temporal to the fovea. Our density measurements are consistent with this range. Finally, in the most recent study, Ach et al.[3] measured RPE density in 20 normal eyes, 10 at or below age of 51 years. For these 10, average RPE density across the perifovea (∼2°–10°) was 5091 ± 823 cells/mm², which is statistically not significant from our 3° and 7° measurements. In general, there is a large variation in RPE densities reported from in vivo and histology studies, including in our own study. This variation points to the importance of in vivo measurements that can track individual differences over time and to detect those cellular changes associated with disease, as for example with AMD.[49]

Our density measurements were spaced relatively close (3° and 7°) and, thus, did not lend themselves to test for a retinal eccentricity dependence. Indeed, no statistical significance was found with Voronoi (paired *t*-test, $P = 0.58$) nor power spectra (paired *t*-test, $P = 0.92$) measurements. We also tested for an age dependence across the age range examined: 25 to 61 years. The regression line in Figure 10 shows a decrease in density with age, but this was not statistically significant ($P = 0.30$). No statistical significance also was found for the corresponding power spectra measurements, but the P value was lower ($P = 0.11$) and the 95% confidence interval for the regression slope was −56.3 to 7.09 cells/mm²/y. The statistical power of just six subjects used in the present study obviously is limited, but the fact that we have demonstrated that RPE packing now is measureable in younger and older eyes establishes a clear path for testing aging effects in a larger population. Such tests have not been conducted in vivo (regardless of imaging modality) and may shed important insight into the aging controversy reported with histologic studies. These studies have reported densities showing no

change with age,[48] a decrease with age,[47,50,51] or different aging effects depending on retinal location.[3,52–55]

Finally, we examined RPE cell regularity. From Voronoi analysis (Fig. 8), the most prevalent number of nearest neighbors regardless of subject and retinal eccentricity was six. Prevalence for six neighbors was 50.49 ± 3.66% at 3° (843 of 1659 cells) and 54.58 ± 3.01% at 7° (733 of 1338 cells), both consistent with histology in humans[3] (49.63 ± 8.74% for ≤51 years group). Prevalence of six neighbors was significantly larger than the next two most prevalent associations: five ($P < 0.05$, *t*-test) and seven ($P < 0.05$, *t*-test). By grouping the three youngest (average = 30.3 years) and three oldest (average = 48.3 years) subjects, prevalence of six nearest neighbors decreased from 52.8% to 51.2% with age. This corresponds to a decrease of approximately 124 RPE cells with six nearest neighbors. This suggestive decrease in cell regularity with age is consistent with the findings of Ach et al.[3] using the same Voronoi metric, but a larger sample size is required to test. Other Voronoi metrics may be more sensitive to packing regularity. For example, the mean standard deviation of the Voronoi side lengths (Fig. 8B) indicates a gradual increase with age ($P = 0.05$), which points to a decrease in cell regularity.

Cone-to-RPE Ratio

Our AO-OCT method captures volume images of the retina and, thus, other layers can be extracted from the same volume, enabling a direct spatial comparison on a cell by cell basis. Figure 6 illustrates this for the spatial arrangement of cone photoreceptors relative to the underlying RPE cells of one subject and Figure 10 quantifies the ratio of these two cell types for all six subjects and two retinal eccentricities. Unlike RPE cell density, which showed no significant difference between 3° and 7°, cone-to-RPE ratio did. The ratio was significantly lower at 7° (2.31 ± 0.23:1) than at 3° (3.78 ± 0.53:1; $P < 0.05$), a factor of 1.6 decrease. This decrease originates from the reduced cone density at the larger retinal eccentricity. For our six subjects, average cone density decreased by a factor of 1.64, close to the 1.6 decrease in cone-to-RPE ratio.

We found limited histologic human data in the literature to compare to our ratio measurements. Gao et al.[51] reported ratios of 24.09:1 at the fovea and 0.89:1 at the equator. Our 3° and 7° ratios fall within this range. Panda-Jonas et al.[47] reported an average cone-to-RPE ratio of 1.10 ± 0.24 across the temporal meridian from approximately 6.7° to 16.7°. Our 7° ratio is a factor of two higher, a portion of which was attributable to the decrease in cone density with retina eccentricity.

We know of no in vivo human data to compare to our present study. For nonhuman primates, Morgan et al.[15] reported in vivo measurements in two macaques, one at 4.5° nasal, 4.5° inferior (5.43:1), and another at 6° temporal, 4.5° superior (4.08:1). This time, our 7° ratio is a factor of two lower. Differences between these measurements and in the present study include differences in subjects, retina locations, and primate species.

Conclusions

We present, to our knowledge, the first detailed characterization of the 3D reflectance profile of individual RPE cells and their surrounding complex in the living human retina. This was made possible using state-of-the-art technology in AO and OCT, but equally critical novel contrast enhancement of the RPE cell based on its own naturally occurring organelle motion. While AO-OCT remains primarily a laboratory method with promise of a clinical one, the most immediate impact is through our retinal findings. Because our method is based on OCT, our measurements represent a valuable resource for interpreting the photoreceptor and RPE bands in clinical OCT.

Acknowledgments

The authors thank Kazuhiro Kurokawa and Furu Zhang for helpful discussions of the manuscript. Financial support was provided by grants from NEI R01 EY018339 and P30 EY019008.

Disclosure: **Z. Liu,** None; **O.P. Kocaoglu,** None; **D.T. Miller,** None

References

1. Strauss O. The retinal pigment epithelium in visual function. *Physiol Rev*. 2005;85:845–881.
2. Boulton ME. Aging of the retinal pigment epithelium. In: Tombran-Tink J, Barnstable C, eds. *Visual Transduction and Non-Visual Light Perception*. New York, NY: Humana Press; 2008:403–420.
3. Ach T, Huisingh C, McGwin G, et al. Quantitative autofluorescence and cell density maps of the human retinal pigment epithelium. *Invest Ophthalmol Vis Sci*. 2014;55:4832–4841.
4. Ach T, Tolstik E, Messinger JD, et al. Lipofuscin re-distribution and loss accompanied by cytoskeletal stress in retinal pigment epithelium of eyes with age-related macular degeneration. *Invest Ophthalmol Vis Sci*. 2015;55:3242–3252.
5. Delori F, Greenberg JP, Woods RL, et al. Quantitative measurements of autofluorescence with the scanning laser ophthalmoscope. *Invest Ophthalmol Vis Sci*. 2011;52:9379–9390.
6. Elsner AE, Burns SA, Weiter JJ, Delori FC. Infrared imaging of sub-retinal structures in the human ocular fundus. *Vision Res*. 1996;36:191–205.
7. Elsner AE, Miura M, Burns SA, et al. Multiply scattered light tomography and confocal imaging: detecting neovascularization in age-related macular degeneration. *Opt Express*. 2000;7:95–106.
8. Elsner AE, Zhou Q, Beck F, et al. Detecting AMD with multiply scattered light tomography. *Int Ophthalmol*. 2001;23:245–250.
9. Burns SA, Elsner AE, Mellem-Kairala MB, Simmons RB. Improved contrast of subretinal structures using polarization analysis. *Invest Ophthalmol Vis Sci*. 2003;44:4061–4068.
10. Mellem-Kairala MB, Elsner AE, Weber A, Simmons RB, Burns SA. Improved contrast of peripapillary hyperpigmentation using polarization analysis. *Invest Ophthalmol Vis Sci*. 2005;46:1099–1106.
11. Ahlers C, Gotzinger E, Pircher M, et al. Imaging of the retinal pigment epithelium in age-related macular degeneration using polarization-sensitive optical coherence tomography. *Invest Ophthalmol Vis Sci*. 2010;51:2149–2157.
12. Schlanitz FG, Baumann B, Spalek T, et al. Performance of automated drusen detection by polarization-sensitive optical coherence tomography. *Invest Ophthalmol Vis Sci*. 2011;52:4571–4579.
13. Gotzinger E, Pircher M, Geitzenauer W, et al. Retinal pigment epithelium segmentation by polarization sensitive optical coherence tomography. *Opt Express*. 2008;16:16410–16422.
14. Yang Q, Reisman CA, Chan KP, et al. Automated segmentation of outer retinal layers in macular OCT images of patients with retinitis pigmentosa. *Biomed Opt Express*. 2011;2:2493–2503.
15. Morgan JI, Dubra A, Wolfe R, Merigan WH, Williams DR. In vivo autofluorescence imaging of the human and macaque retinal pigment epithelial cell mosaic. *Invest Ophthalmol Vis Sci*. 2009;50:1350–1359.

16. Roorda A, Zhang Y, Duncan JL. High-resolution in vivo imaging of the RPE mosaic in eyes with retinal disease. *Invest Ophthalmol Vis Sci*. 2007;48:2297–2303.
17. Chui TYP, Zhong ZY, Burns SA. The relationship between peripapillary crescent and axial length: implications for differential eye growth. *Vision Res*. 2011;51:2132–2138.
18. Gray DC, Merigan W, Wolfing JI, et al. In vivo fluorescence imaging of primate retinal ganglion cells and retinal pigment epithelial cells. *Opt Express*. 2006;14:7144–7158.
19. Scoles D, Sulai YN, Dubra A. In vivo dark-field imaging of the retinal pigment epithelium cell mosaic. *Biomed Opt Express*. 2013;4:1710–1723.
20. Torti C, Povazay B, Hofer B, et al. Adaptive optics optical coherence tomography at 120,000 depth scans/s for non-invasive cellular phenotyping of the living human retina. *Opt Express*. 2009;17:19382–19400.
21. Felberer F, Kroisamer JS, Baumann B, et al. Adaptive optics SLO/OCT for 3D imaging of human photoreceptors in vivo. *Biomed Opt Express*. 2014;5:439–456.
22. Staurenghi G, Sadda S, Chakravarthy U, Spaide RF. International nomenclature for optical coherence tomography P. Proposed lexicon for anatomic landmarks in normal posterior segment spectral-domain optical coherence tomography: the IN*OCT consensus. *Ophthalmology*. 2014;121:1572–1578.
23. Liu Z, Kocaoglu OP, Miller DT. In-the-plane design of an off-axis ophthalmic adaptive optics system using toroidal mirrors. *Biomed Opt Express*. 2013;4:3007–3029.
24. Shafer BA, Kriske JE, Kocaoglu OP, et al. Adaptive-optics optical coherence tomography processing using a graphics processing unit. *Conf Proc IEEE Eng Med Biol Soc*. 2014; 3877–3880.
25. Kriske JE. *A Scalable Approach to Processing Adaptive Optics Optical Coherence Tomography Data from Multiple Sensors Using Multiple Graphics Processing Units* [master's thesis] West Lafayette, IN: Purdue University; 2014.
26. Bennett AG, Rudnicka AR, Edgar DF. Improvements on Littmann method of determining the size of retinal features by fundus photography. *Graefes Arch Clin Exp Ophthalmol*. 1994;232:361–367.
27. ANSI Z136.1 – 2014. American National Standard for Safe Use of Lasers. Orlando, FL: Laser Institute of America; 2014.
28. Weiter JJ, Delori FC, Wing GL, Fitch KA. Retinal-pigment epithelial lipofuscin and melanin and choroidal melanin in human eyes. *Invest Ophthalmol Vis Sci*. 1986;27:145–152.
29. Delori FC, Goger DG, Dorey CK. Age-related accumulation and spatial distribution of lipofuscin in RPE of normal subjects. *Invest Ophthalmol Vis Sci*. 2001;42:1855–1866.
30. Spaide RF, Curcio CA. Anatomical correlates to the bands seen in the outer retina by optical coherence tomography literature review and model. *Retina-J Ret Vit Dis*. 2011;31:1609–1619.
31. Jonnal RS, Kocaoglu OP, Zawadzki RJ, et al. The cellular origins of the outer retinal bands in optical coherence tomography images. *Invest Ophthalmol Vis Sci*. 2014;55:7904–7918.
32. Jonnal RS, Kocaoglu OP, Wang Q, Lee S, Miller DT. Phase-sensitive imaging of the outer retina using optical coherence tomography and adaptive optics. *Biomed Opt Express*. 2012;3: 104–124.
33. Kocaoglu OP, Ferguson RD, Jonnal RS, et al. Adaptive optics optical coherence tomography with dynamic retinal tracking. *Biomed Opt Express*. 2014;5:2262–2284.
34. Liu Z, Kocaoglu OP, Turner TL, Miller DT. Modal content of living human cone photoreceptors. *Biomed Opt Express*. 2015;6:3378–3404.
35. Curcio CA, Sloan KR, Kalina RE, Hendrickson AE. Human photoreceptor topography. *J Comp Neurol*. 1990;292:497–523.
36. Kocaoglu OP, Lee S, Jonnal RS, et al. Imaging cone photoreceptors in three dimensions and in time using ultrahigh resolution optical coherence tomography with adaptive optics. *Biomed Opt Express*. 2011;2:748–763.
37. Lee SH, Werner JS, Zawadzki RJ. Improv ed visualization of outer retinal morphology with aberration cancelling reflective optical design for adaptive optics - optical coherence tomography. *Biomed Opt Express*. 2013;4:2508–2517.
38. Zhang Y, Cense B, Rha J, et al. High-speed volumetric imaging of cone photoreceptors with adaptive optics spectral-domain optical coherence tomography. *Opt Express*. 2006;14:4380–4394.
39. Srinivasan VJ, Monson BK, Wojtkowski M, et al. Characterization of outer retinal morphology with high-speed, ultrahigh-resolution optical coherence tomography. *Invest Ophthalmol Vis Sci*. 2008;49:1571–1579.
40. Hoang QV, Linsenmeier RA, Chung CK, Curcio CA. Photoreceptor inner segments in monkey and human retina: mitochondrial density, optics, and regional variation. *Vis Neurosci*. 2002;19:395–407.
41. Dunn AK, Smithpeter CL, Welch AJ, Richards-Kortum RR. Finite-difference time-domain simulation of light scattering from single cells. *J Biomed Opt*. 1997;2:262–266.
42. Starnes AC, Huisingh C, McGwin G Jr, et al. Multi-nucleate retinal pigment epithelium cells of the human macula exhibit a characteristic and highly specific distribution. *Vis Neurosci*. 2016;33:e001.
43. Krebs W, Krebs IP. Quantitative morphology of the central fovea in the primate retina. *Am J Anat*. 1989;184:225–236.
44. Keilhauer CN, Delori FC. Near-infrared autofluorescence imaging of the fundus: visualization of ocular melanin. *Invest Ophthalmol Vis Sci*. 2006;47:3556–3564.
45. Baumann B, Baumann SO, Konegger T, et al. Polarization sensitive optical coherence tomography of melanin provides intrinsic contrast based on depolarization. *Biomed Opt Express*. 2012;3:1670–1683.
46. Song HX, Chui TYP, Zhong ZY, Elsner AE, Burns SA. Variation of cone photoreceptor packing density with retinal eccentricity and age. *Invest Ophthalmol Vis Sci*. 2011;52:7376–7384.
47. Panda-Jonas S, Jonas JB, Jakobczyk-Zmija M. Retinal pigment epithelial cell count, distribution, and correlations in normal human eyes. *Am J Ophthalmol*. 1996;121:181–189.
48. Watzke RC, Soldevilla JD, Trune DR. Morphometric analysis of human retinal-pigment epithelium - correlation with age and location. *Curr Eye Res*. 1993;12:133–142.
49. Rossi EA, Rangel-Fonseca P, Parkins K, et al. In vivo imaging of retinal pigment epithelium cells in age related macular degeneration. *Biomed Opt Express*. 2013;4:2527–2539.
50. Dorey CK, Wu G, Ebenstein D, Garsd A, Weiter JJ. Cell loss in the aging retina. Relationship to lipofuscin accumulation and macular degeneration. *Invest Ophthalmol Vis Sci*. 1989;30: 1691–1699.
51. Gao H, Hollyfield JG. Aging of the human retina - differential loss of neurons and retinal-pigment epithelial-cells. *Invest Ophthalmol Vis Sci*. 1992;33:1–17.
52. Ts'o MM, Friedman E. The retinal pigment epithelium: III. growth and development. *Arch Ophthalmol*. 1968;80:214–216.
53. Harman AM, Fleming PA, Hoskins RV, Moore SR. Development and aging of cell topography in the human retinal pigment epithelium. *Invest Ophthalmol Vis Sci*. 1997;38:2016–2026.
54. Del Priore LV, Ku YH, Tezel TH. Age-related changes in human RPE cell density and apoptosis proportion in situ. *Invest Ophthalmol Vis Sci*. 2002;43:3312–3318.
55. Streeten BW. Development of the human retinal pigment epithelium and the posterior segment. *Arch Ophthalmol*. 1969;81:383–394.

Investigative Ophthalmology & Visual Science